THE JOURNAL OF PHYSICAL CHEMISTRY C

pubs.acs.org/JPCC Article

Deciphering the Nature of Ru Sites in Reductively Exsolved Oxides with Electronic and Geometric Metal−Support Interactions

Muhammad A. Naeem, Dudari B. Burueva, Paula M. Abdala, Nikolai S. Bushkov, Dragos Stoian, Andrey V. Bukhtiyarov, Igor P. Prosvirin, Valerii I. Bukhtiyarov, Kirill V. Kovtunov, Igor V. Koptyug, Alexey Fedorov,* and Christoph R. Müller*

Cite This: J. Phys. Chem. C 2020, 124, 25299−25307 Read Online

ACCESS | Metrics & More | Article Recommendations | Supporting Information

ABSTRACT: The reductive exsolution of metallic Ru from fluorite-type solid solutions $Ln_2Ru_{0.2}Ce_{1.8}O_7$ (Ln = Sm, Nd, La) leads to materials with metal−support interactions that influence the electronic state and the catalytic activity of Ru. In situ X-ray absorption spectroscopy at the Ru K-edge identified that with increasing temperature, the exsolution of Ru from $Sm_2Ru_{0.2}Ce_{1.8}O_7$ in a H_2 atmosphere proceeds via an intermediate $Ru^{\delta+}$ state, that is, $Ru^{4+}\rightarrow Ru^{\delta+}\rightarrow Ru^0$. X-ray photoelectron spectroscopy (XPS) established that, in parallel (H_2 atmosphere at ca. 500 °C), also Ce^{4+} ions reduce to Ce^{3+}, which is accompanied by an electron transfer from the reduced host oxide to the exsolved Ru^0 clusters, creating $Ru^{\delta-}$ states. Low-temperature diffuse reflectance infrared Fourier transform spectroscopy (DRIFTS) using CO as a probe molecule reveals a red shift of the CO adsorption bands by ca. 18 cm^{-1} when increasing the temperature during the H_2 treatment from 300 to 500 °C, consistent with an increased π-backdonation from more electron-rich Ru species to CO. However, at a lower reduction temperature of ca. 100 °C, a blue-shifted CO band is observed that is explained by a Lewis-acidic $Ru^{\delta+}$−CO adduct. Nuclear magnetic resonance (NMR) signal enhancement in parahydrogen-induced polarization experiments was used as a structure-sensitive probe and revealed a decreasing propene hydrogenation rate with increasing exsolution temperature, accompanied by a notable enhancement of propane hyperpolarization (ca. 3-fold higher at 500 °C than at 300 °C). These data suggest that the exsolved, subnanometer-sized Ru species are more active in propene hydrogenation but less selective for the pairwise addition of p-H_2 to propene than $Ru^{\delta-}$ sites engaged in a strong metal−support interaction.

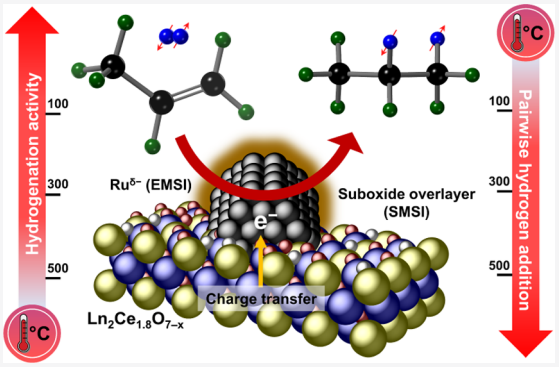

1. INTRODUCTION

Model catalysts containing oxide-supported well-defined and highly dispersed metallic nanoparticles of controllable size, shape, particle size distribution, and composition have been instrumental in advancing our understanding of various essential catalytic processes.[1−5] One of the key challenges in the development of such model catalysts has been controlling simultaneously the density and size of the supported nanoparticles, their uniform distribution, and metal−support interaction (MSI).[6−10] Recently, exsolution of metal nanoparticles (Pd, Rh, Pt, Ni, Co, Fe) from a host oxide lattice in a reductive H_2 atmosphere has emerged as a powerful method to produce model heterogeneous catalysts,[11−18] often yielding materials with a narrow particle size distribution and stabilizing MSI.[14,19−21] Such MSIs can be categorized as follows: (i) electronic interactions including, for instance, charge transfer at the metal−support interface (EMSI)[22,23] that can alter the electronic state of supported nanoparticles or clusters[24,25] or (ii) geometric MSI resulting in a partial confinement (i.e., oxide overcoat, SMSI) of the supported species by the reduced support.[6,26] Those two types of MSIs are often entangled and govern the catalytic activity and selectivity of the material by affecting the adsorption energy and surface diffusion of reaction intermediates.[27−30]

Recent reports demonstrated that the effects of MSI on the pairwise selectivity of parahydrogen (p-H_2) addition in hydrogenation reactions are strongly dependent on the specific catalyst system and the respective electronic state of the active sites, influenced by SMSI and/or EMSI. For instance, an enhanced pairwise selectivity was observed over Ir/TiO_2 due to the formation of electron-rich Ir species generated during the reduction at 500 °C.[31] In contrast, a $Pd^{\delta+}$ electronic state was obtained in Pd/TiO_2 when reduced in hydrogen at 500 °C and showed an overall decreased activity and pairwise addition selectivity.[29] Therefore, to establish a general framework of the

Received: August 6, 2020
Revised: October 3, 2020
Published: November 10, 2020

effects of MSI on activity and pairwise selectivity, a broader survey of other supported metal catalysts is necessary. Here, we aim to probe supported Ru-based catalysts synthesized via a reductive exsolution approach, assess the associated MSI phenomena, and perform a structure−activity study of the exsolved materials for the hydrogenation of propene with p-H_2 (a model reaction).

The applied conditions during reductive exsolution play a major role in controlling the resulting particle size and the nature of the metal−support interaction (geometric and electronic).[31−33] For example, we have recently reported that the reductive exsolution of metallic Ru from fluorite-type $Sm_2Ru_xCe_{2-x}O_7$ solid solutions yields, at 700 °C, highly dispersed supported metallic nanoparticles of ca. 1 nm in diameter that are socketed in the host oxide surface.[34] This type of strong MSI reduced the mobility of the exsolved nanoparticles under the high-temperature conditions in the dry reforming of methane (DRM) and thereby moderated sintering of the active component, which is a typical deactivation route of DRM catalysts. In contrast, here, we focus on understanding the nature of Ru and the support surface during the reductive exsolution of metallic Ru from $Ln_2Ru_{0.2}Ce_{1.8}O_7$ (Ln = Sm, Nd, La) in a lower temperature range, i.e., ca. 25−500 °C, using a combination of bulk and surface-sensitive characterization techniques including in situ X-ray diffraction (XRD)−X-ray absorption spectroscopy (XAS), X-ray photoelectron spectroscopy (XPS), Raman spectroscopy, CO-diffuse reflectance infrared Fourier transform spectroscopy (DRIFTS), H_2-temperature-programmed desorption (H_2-TPD), and transmission electron microscopy (TEM). Ru K-edge XAS data show that Ru exsolves from the parent solid solution phase through an intermediate $Ru^{\delta+}$ state, that is, $Ru^{4+}\rightarrow Ru^{\delta+}\rightarrow Ru^0$. Following the atomic ratio of Ru/Ce, Ru/Ln, and Ru/(Ce+Ln) by XPS as a function of reduction temperature, already at 100 °C, a maximum in the Ru surface concentration is observed; increasing the temperature further lowers the Ru/Ce and Ru/Ln ratios, consistent with the geometric SMSI. The XPS analysis also demonstrated that the reduction of $Ln_2Ru_{0.2}Ce_{1.8}O_7$ in H_2 at ca. 300−500 °C yields electron-rich $Ru^{\delta-}$ states owing to the charge transfer (electronic MSI) from the reduced support to the exsolved material.

This is further corroborated by DRIFTS results using CO as the probe molecule, revealing an increasing red shift of bound CO, and hence a more electron-rich Ru^0 surface, with an increasing reduction temperature. Finally, the hydrogenation of propene with p-H_2, which leads to a nuclear magnetic resonance (NMR) signal enhancement of the hydrogenation product propane, provided a structure-sensitive reaction,[35−37] allowing us to assess the interplay between the electronic and geometric MSIs of supported Ru species.[38,39] Specifically, we find that the selectivity of the pairwise addition of p-H_2 to propene is influenced strongly by the nature of the Ru sites. We observed an up to 3-fold increase in propane polarization on electron-rich $Ru^{\delta-}$ species that are in electronic and geometric MSI with the support compared to Ru^0 species (Figure 1). Yet the catalytic activity of $Ru^{\delta-}$ is lower than that of Ru^0, likely owing to the blocking of active Ru sites by reduced Ce^{3+} sites.

2. EXPERIMENTAL METHODS

2.1. Material Characterization. Details on N_2 physisorption, laboratory-based XRD measurements, CO-DRIFTS, XPS, H_2-TPD, Ru K-edge XAS, and Raman spectroscopy are provided in the Supporting Information.

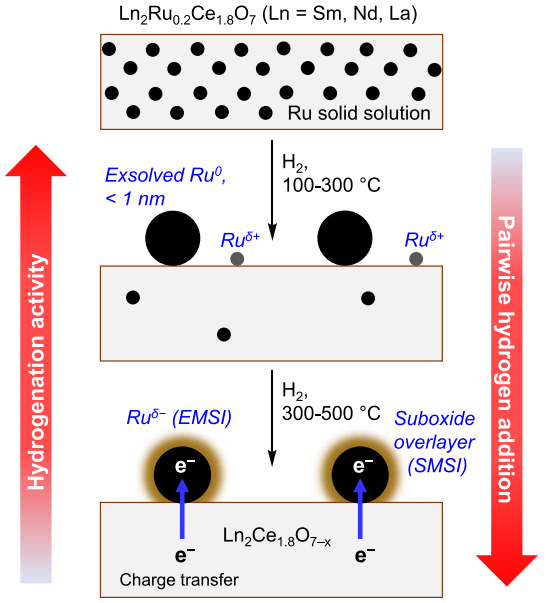

Figure 1. Schematic of the reductive exsolution of Ru from $Ln_2Ru_{0.2}Ce_{1.8}O_7$ associated with electronic and geometric metal−support interactions (EMSI and SMSI, respectively) and its effect on the catalytic performance in propene hydrogenation.

3. RESULTS AND DISCUSSION

$Ln_2Ru_{0.2}Ce_{1.8}O_7$ (Ln = Sm, Nd, La) solid solutions were prepared following a general protocol described by us recently (see the Supporting Information for details).[34] For brevity, in what follows, we focus on $Sm_2Ru_{0.2}Ce_{1.8}O_7$ (Figure 2a) as a representative material, while experimental results for $Nd_2Ru_{0.2}Ce_{1.8}O_7$ and $La_2Ru_{0.2}Ce_{1.8}O_7$ are presented in the Supporting Information. The structural evolution of $Sm_2Ru_{0.2}Ce_{1.8}O_7$ under reductive conditions (10 vol % H_2 in N_2, 1 bar) was probed by in situ combined XRD and XAS (Ru K-edge) in a temperature programmed reduction (TPR) experiment (25−700 °C).[34,40,41] With increasing temperature, a decrease of the white line intensity and a gradual shift of the absorption edge toward lower energies are observed in the X-ray absorption near-edge structure (XANES) spectra of $Sm_2Ru_{0.2}Ce_{1.8}O_7$. Such changes are consistent with the gradual reduction of Ru (Figure 2b). At 460 °C, the position of the absorption edge of $Sm_2Ru_{0.2}Ce_{1.8}O_{7(460\text{-}H2)}$ and its pre-edge features are similar to the reference Ru foil, indicating that a major fraction of Ru was reduced to the metallic Ru. Likewise, in the extended X-ray absorption fine structure (EXAFS) data, the amplitude of the peak due to the Ru−O coordination sphere decreases continuously with increasing temperature (Figure 2c). This reduction in amplitude is due to both a decrease in the coordination number related to the reduction of the oxide solid solution and an increase in the (thermal) disorder. At 500 °C, in the FT of the EXAFS data, a peak develops at ca. 2.4 Å, which is due to the formation of a Ru−Ru shell in Ru^0. Next, we applied a principal component analysis (PCA) to the in situ XANES spectra, which indicated that the reduction is described well by three main components (see the Supporting Information for details). To deconvolute the spectra and their evolution with temperature during the in situ TPR, multivariate curve resolution−alternating least-

https://dx.doi.org/10.1021/acs.jpcc.0c07203
J. Phys. Chem. C 2020, 124, 25299−25307

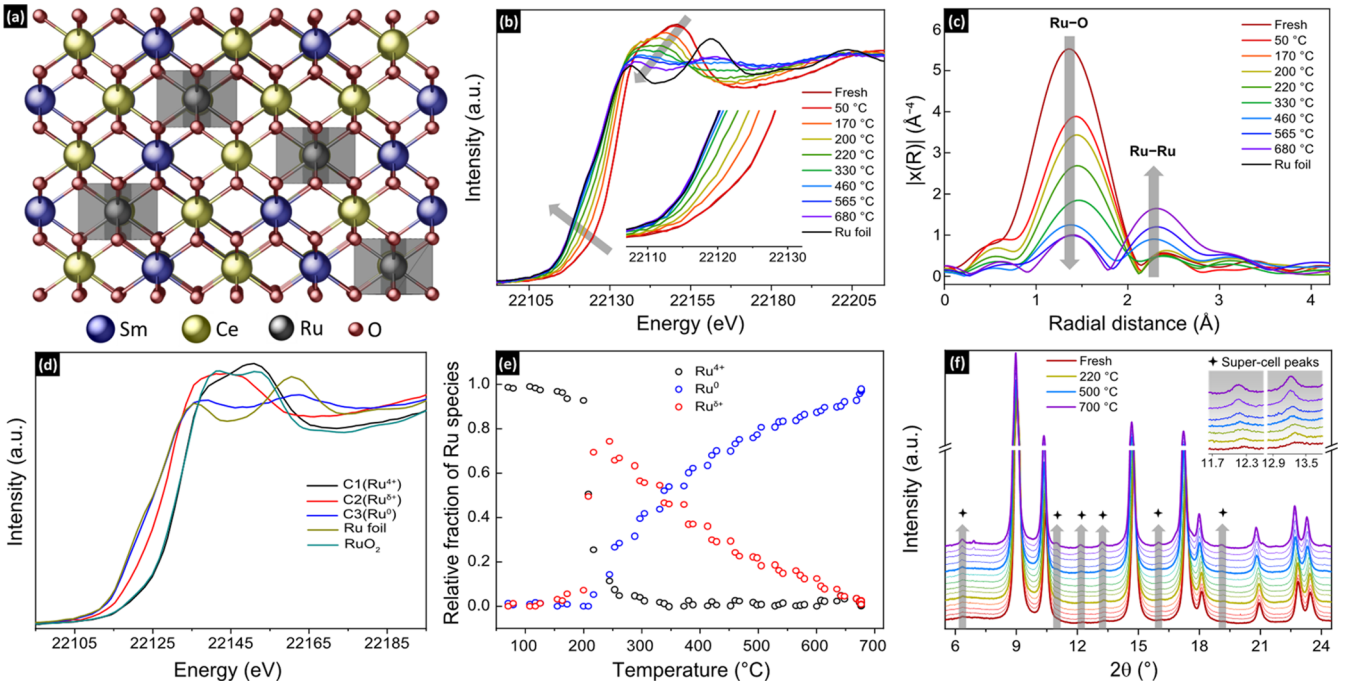

Figure 2. (a) Illustration of the crystal structure of fluorite $Sm_2Ru_{0.2}Ce_{1.8}O_7$ solid solution (Sm and Ru atoms substitute Ce position in the lattice). (b) Normalized Ru K-edge XANES spectra and (c) Fourier transforms of k^3-weighted EXAFS data of the in situ TPR experiment (conditions 10% H_2 in N_2). (d) XANES spectra of C1, C2, and C3 components extracted from MCR-ALS analysis, attributed to Ru^{4+}, $Ru^{\delta+}$, and Ru^0. (e) MCR-ALS analysis of the Ru K-edge XANES data as a function of reduction temperature and (f) in situ XRD (λ = 0.49751 Å) patterns of $Sm_2Ru_{0.2}Ce_{1.8}O_7$ obtained during the same TPR experiment.

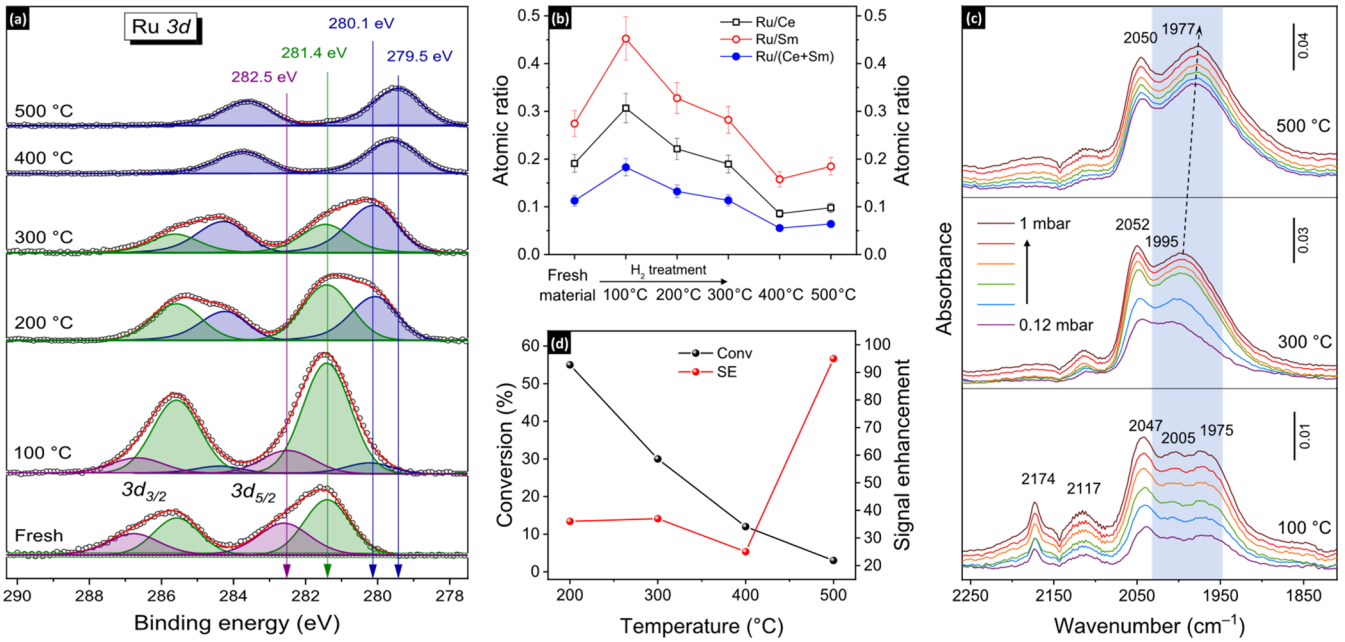

Figure 3. (a) Deconvolution of the XPS data at the Ru 3d core level and (b) atomic ratios of Ru/Ce, Ru/Sm, and Ru/(Ce+Sm) for $Sm_2Ru_{0.2}Ce_{1.8}O_7$ in calcined and reduced states (the standard error for quantitative analysis was within 10%). (c) Comparison of the in situ CO-DRIFT spectra measured at −25 °C for $Sm_2Ru_{0.2}Ce_{1.8}O_7$ after reductive treatment in 10 vol % H_2 in N_2 for 30 min at 100, 300, or 500 °C. The trace label shows the CO partial pressure. (d) Temperature dependence of propene conversion and propane NMR signal enhancement (SE) for $Sm_2Ru_{0.2}Ce_{1.8}O_7$ (C_3H_6/p-H_2 = 1:4; total flow, 3.8 mL s^{-1}; $Sm_2Ru_{0.2}Ce_{1.8}O_7$, 30 mg).

squares (MCR-ALS) analysis was applied.[40] The MCR-ALS analysis was performed assuming that the data can be described sufficiently by three components, as suggested by the PCA analysis. Components 1 and 3 extracted by the MCR-ALS analysis match well the spectra of $Sm_2Ru_{0.2}Ce_{1.8}O_7$ (Ru^{4+} oxidation state) and metallic Ru, respectively, while we ascribe component 2 to an intermediate oxidation state of Ru, i.e., a $Ru^{\delta+}$ state (Figures 2d and S1–S3). According to the concentration profile (i.e., a fraction of Ru species as a function of temperature) obtained through the MCR-ALS

https://dx.doi.org/10.1021/acs.jpcc.0c07203
J. Phys. Chem. C 2020, 124, 25299−25307

analysis, the intermediate $Ru^{\delta+}$ state reaches a maximal weight fraction of 0.7 already at 230 °C and then decreases to its minimum at 680 °C. The fitting of the EXAFS data allowed the determination of the variation of the interatomic Ru−O distances as a function of reduction temperature. The Ru−O interatomic distances increase from 1.96(6) to 2.02(7) Å between ca. 200 and 250 °C (Figure S9a and Table S3), which correlates with the presence of an intermediate $Ru^{\delta+}$ state determined by the MCR-ALS analysis of the XANES data (Figure 2e). According to the MCR-ALS analysis, metallic Ru starts to appear at ca. 220 °C and its weight fraction reaches ca. 0.8 at 500 °C and continues to increase up to 680 °C (Figure 2e). The XRD data collected during the same experiment reveal the onset of supercell Bragg reflections, typical for $Sm_2Ce_2O_7$ that crystallizes in a C-type phase, at ca. 220 °C (Figure 2f). The presence of peaks due to the $Sm_2Ce_2O_7$ phase confirms that the exsolution of Ru from $Sm_2Ru_{0.2}Ce_{1.8}O_7$ triggers a fluorite-to-C-type transition that is characterized by a rearrangement of oxygen vacancies.[42] No XRD peaks related to metallic Ru are observed up to 700 °C, which suggests the formation of highly dispersed Ru nanoclusters on the surface of the $Sm_2Ce_{1.8}O_{7-\delta}$ support.[34] The EXAFS fittings reveal that the Ru−Ru coordination number for $Sm_2Ru_{0.2}Ce_{1.8}O_{7(700\text{-}H2)}$ (collected after cooling down to 50 °C in situ) is 6.9(1) (Table S4c and Figure S10c), which is indeed consistent with the exsolution of Ru nanoparticles of ca. 1 nm in diameter[34] under these conditions.[43] These results are in line with the observations made by scanning transmission electron microscopy (STEM) (Figure S9b,c).

XPS spectra of calcined $Sm_2Ru_{0.2}Ce_{1.8}O_7$ and of reduced samples (at 100, 200, 300, 400, and ca. 500 °C for 1 h for each reduction temperature and at 300 mbar H_2) were acquired to assess the electronic states of the exsolved Ru surface species and to probe for metal−support interactions. Core-level Ru 3d spectra feature a doublet corresponding to the Ru $3d_{5/2}$ and Ru $3d_{3/2}$ states due to spin−orbit splitting. Calcined $Sm_2Ru_{0.2}Ce_{1.8}O_7$ exhibits two deconvolved Ru $3d_{5/2}$ core peaks at binding energies (BE) of 282.5 and 281.4 eV, corresponding to the Ru^{4+} state and Ru in a lower oxidation state, denoted as a $Ru^{\delta+}$ state.[44−47] We note that a $Ru^{\delta+}$ state with a BE of 281.4 eV has been ascribed previously to Ru^{2+} cationic species.[46,48,49] Notably, in comparison to Ru K-edge XANES (i.e., a bulk probe used at 1 bar), a higher fraction of surface $Ru^{\delta+}$ species was detected by XPS analysis. This difference can be explained by the surface sensitivity (sampling depth, ca. 40−45 Å) of XPS and the use of high vacuum. Reduction at 100 °C yields a small peak at 280.1 eV that is characteristic of metallic ruthenium (Figures 3a and S4a).[50,51] The intensity of the Ru^0 peak at 280.1 eV grows gradually with increasing reduction temperature (up to 300 °C). At this temperature, Ru^0 and $Ru^{\delta+}$ states coexist (major and minor components, respectively) while no Ru^{4+} state is present. The evolution of metallic and oxidized Ru species as a function of the reduction temperature indicates that at ca. 400 °C, all surface Ru is metallic (Figures 3a and S11). XPS data also reveal a notable shift of the Ru^0 peak position to lower BE with increasing reduction temperature. Specifically, a shift by ca. 0.6 eV to lower energies of the Ru^0 state is observed when comparing the XPS spectra at 300 and 400 or 500 °C (i.e., the BE position of metallic Ru shifted from 280.1 to 279.5 eV when the temperature was increased from 300 to 500 °C). This effect can be explained by an altered electronic structure of metallic Ru due to alloying with a metal of the reduced oxide support[52,53] or a charge transfer from the reduced support to the exsolved metal.[52,54,55]

In contrast to the reported XANES data on intermetallic compounds of Ru with rare-earth metals (e.g., YRu_2) that exhibit an ca. 2 eV shift toward lower edge energies relative to Ru^0,[56] we observe no such shift to lower energies in the Ru K-edge XANES data of exsolved $Sm_2Ru_{0.2}Ce_{1.8}O_7$ at least up to 700 °C (Figure 2b), suggesting that the formation of Ru−Ce/Sm intermetallics is unlikely under these conditions. The decrease of the work function of metallic ruthenium owing to the transfer of electron density from the reduced support to Ru^0 was previously reported.[57−59] This precedent points to an electronic metal−support interaction via charge transfer and also indicates that the state of Ce was modified after the reduction step, which facilitated the observed EMSI.[60−63] Indeed, while the Ce 3d XPS spectrum of calcined $Sm_2Ru_{0.2}Ce_{1.8}O_7$ shows a predominant Ce^{4+} state, reduction at 500 °C transforms Ce^{4+} to the Ce^{3+} state, as suggested by the emergence of broad shoulder peaks at BEs of ca. 885 and 903 eV,[64] respectively (Figures S12a and S13). That being said, the corresponding 3d XPS spectra of Sm do not show a notable change of the Sm^{3+} state, which makes Ce^{3+} ions a likely source of electrons for the $Ru^{\delta-}$ species (Figure S12b). These results suggest that the high reduction temperature (ca. 500 °C) is the key parameter for establishing an EMSI effect leading to $Ru^{\delta-}$ species.[53−55,62,63] XPS results revealed that the atomic ratio of Ru/Ce at the surface is higher in the calcined solid solution relative to the nominal bulk ratio (i.e., 0.2/1.0 and 0.2/1.8, respectively). This suggests a higher concentration of Ru cations in surface layers of $Sm_2Ru_{0.2}Ce_{1.8}O_7$ relative to the bulk concentration of Ru. Following the evolution of the Ru, Ce and Sm surface species in $Sm_2Ru_{0.2}Ce_{1.8}O_7$ as a function of the reduction temperature shows that the Ru/(Ce+Sm) ratio reaches its maximum already at 100 °C and then gradually decreases up to 400 °C, indicative of a geometric MSI due to the particle encapsulation of Ru (overcoating) by $Sm_2Ce_{1.8}O_{7-\delta}$ (Figure 3b).[2,6,26,65] Thus, the influence of the geometric and electronic MSI effects on the state of Ru (and ultimately, its catalytic properties, vide infra) is entangled in the present system. Notably, $Nd_2Ru_{0.2}Ce_{1.8}O_7$ and $La_2Ru_{0.2}Ce_{1.8}O_7$ behave similarly to $Sm_2Ru_{0.2}Ce_{1.8}O_7$ under reducing conditions (Figures S14−S18).

The effect of MSI on the state of Ru in $Sm_2Ru_{0.2}Ce_{1.8}O_7$ reduced at 300 and 500 °C (5% H_2/Ar) was further elucidated by H_2-TPD experiments.[41] Notably, the amount of released H_2 determined in H_2-TPD experiments decreases from 104 to 96 μmol g^{-1} when increasing the reduction temperature from 300 to 500 °C (Table S5). These data are also consistent with CO-TPD measurements that indicate a decreased CO uptake for $Sm_2Ru_{0.2}Ce_{1.8}O_7$ reduced at 500 °C relative to 300 °C, i.e., 60 and 82 μmol g^{-1}, respectively (Table S5 and Figure S19). This decrease of chemisorbed H_2 and CO can be caused by geometric (encapsulation of active sites) and/or electronic MSI effects, consistent with XPS findings (Figure 3a,b). Note that as the stoichiometry of H_2 chemisorption on $Ru^{\delta-}$ sites is not clear currently, the assessment of the active surface area of $Ru^{\delta-}$ and comparison of the catalytic activity expressed in turnover frequencies (TOF) is unavailable. Thus, the catalytic activity is compared only as conversion and product selectivity (vide infra). As mentioned above, the Ru particle size reaches a diameter of ca. 1 nm after reduction at 700 °C and is likely to be smaller at lower reduction temperatures (Figure S9).

https://dx.doi.org/10.1021/acs.jpcc.0c07203
J. Phys. Chem. C 2020, 124, 25299−25307

DRIFTS experiments using CO as the probe molecule provided additional insights into the chemical state of the exsolved Ru species. Before CO adsorption, the reductive treatment of calcined $Sm_2Ru_{0.2}Ce_{1.8}O_7$ was performed in a Harrick cell with 10% H_2/N_2 (30 mL min^{-1}) at 100, 300, or 500 °C for 30 min, followed by purging with N_2 (10 min, 30 mL min^{-1}) and cooling down in high vacuum. High-purity CO (99.97%) was pulsed to the outgassed specimen at −25 °C to avoid potential oxidation of CO by the material or CO-induced agglomeration and/or restructuring of highly dispersed Ru sites (Figure 3c). The calcined Ru-free $Sm_2Ce_2O_7$ reference material showed no vibrational bands of adsorbed CO species owing to a weak interaction between CO and $Sm_2Ce_2O_7$ (Figure S20a). However, calcined $Sm_2Ru_{0.2}Ce_{1.8}O_7$ exhibited a characteristic low-intensity band of adsorbed CO at 2174 cm^{-1} (no gaseous CO[66] was observed under these conditions; Figure S20b). After reduction at 100 °C, $Sm_2Ru_{0.2}Ce_{1.8}O_7$ features bands of adsorbed CO at 2174, 2117, 2047, 2005, and 1975 cm^{-1}. An increase of the CO partial pressure from 0.12 to 1 mbar did not yield any significant shift of peak maxima positions, and no additional peaks appeared. The band centered at ca. 2174 cm^{-1} is tentatively ascribed to the monocarbonyl species $Ru^{\delta+}(CO)$,[67] while the band at ca. 2117 cm^{-1} is associated with multicarbonyl species on $Ru^{\delta+}$ sites.[67−70] This assignment is consistent with the complete disappearance of the 2174 cm^{-1} band after reduction at 300 °C, along with a notable decrease of the intensity of the 2117 cm^{-1} band at this reduction temperature, as would be expected based on the MCR-ALS analysis of the $Ru^{\delta+}$ sites discussed above. Turning now to the red-shifted CO, the strong band at ca. 2047 cm^{-1} is ascribed to linear CO adsorbed on Ru^0 (i.e., Ru^0−CO),[71−75] while the band at 1975 cm^{-1} can be attributed to bridging CO (i.e., Ru_2^0−CO)[76] and/or linearly bonded CO on the Ru-top site.[77] The band at ca. 2005 cm^{-1} has been observed previously and was attributed to CO adsorbed linearly on high-energy Ru defect sites of smaller crystallites; an alternative assignment is CO adsorbed on isolated Ru^0 atoms surrounded by partially oxidized Ru and/or monocarbonyl CO on partially oxidized Ru (see Table S6 for details).[68,78−80] Generally, the intensities of the CO bands increase with increasing exsolution temperature. Reduction at 300 °C gives two main bands at ca. 2052 and 1995 cm^{-1}. The first band could be a blue-shifted band at 2047 cm^{-1}, while the new band at 1995 cm^{-1} may be attributed to CO on isolated Ru^0 atoms,[81] highlighting the exsolution of highly dispersed Ru^0 sites. At 500 °C, the spectra evolved further, showing main bands at 2050 and 1977 cm^{-1}. Similarly to the band at 1975 cm^{-1} mentioned above, the band at 1977 cm^{-1} can be attributed to bridging Ru_2^0−CO species, possibly at a Ru−support interface.[74,77,82,83] Alternatively, compared to the spectra at 300 °C, the band at 1977 cm^{-1} is red-shifted by 18 cm^{-1} relative to the band at 1995 cm^{-1} and is notably more intense, especially at a low CO pressure. This marked red shift would be consistent with the formation of the electron-rich $Ru^{\delta-}$ state, described above based on the XPS data. The aforementioned assignment of the band at 1977 cm^{-1} to CO on isolated Ru atoms, as was proposed for sites on $Sm_2Ru_{0.2}Ce_{1.8}O_{7(100\text{-}H2)}$, appears less likely for $Sm_2Ru_{0.2}Ce_{1.8}O_{7(500\text{-}H2)}$ owing to the expected formation of larger Ru clusters at higher exsolution temperatures (i.e., 500 °C vs 100 °C). A stronger red-shifted CO band can be expected on more electron-rich, partially negatively charged noble metals that permit more π-backdonation to the CO antibonding orbitals, which weakens the CO molecule.[2,84−86] However, assignment of the 1977 cm^{-1} band to $Ru^{\delta-}$−CO species is tentative.

In summary, DRIFTS experiments with the CO probe molecule are generally consistent with the formation of more electron-rich Ru sites ($Ru^{\delta-}$ surface species) with the reductive treatment of $Sm_2Ru_{0.2}Ce_{1.8}O_7$ at 500 °C (Figure 3a,c). In addition, it is likely that $Ru^{\delta+}$ surface sites only exist at low reduction temperatures (ca. 100 °C) and, by and large, disappear at ca. 300 °C.

We have also verified the surface structure of $Sm_2Ru_{0.2}Ce_{1.8}O_7$ under reductive treatment by in situ Raman spectroscopy. The TPR Raman experiment was performed in a Linkam CCR1000 in situ cell with 10% H_2/N_2 (30 mL min^{-1}) in the temperature range of 25−500 °C (10 °C min^{-1}). The characteristic band of Ru sites in the $Sm_2Ru_{0.2}Ce_{1.8}O_7$ solid solution at ca. 690 cm^{-1} disappears almost entirely already at ca 135 °C (Figure S21). This observation confirms a facile exsolution of the Ru sites in the host oxide lattice, in a good agreement with XAS and XPS data, as discussed above. Importantly, exposure of the in situ reduced $Sm_2Ru_{0.2}Ce_{1.8}O_{7(500\text{-}H2)}$ to air (30 mL min^{-1}, 30 min) at 500 °C leads to a reappearance of the band at ca. 690 cm^{-1}. This indicates that the exsolved Ru can be redissolved reversibly in the host oxide under these conditions.

The gas-phase hydrogenation of propene to propane using p-H_2 under ALTADENA conditions[31] was chosen as a structure-sensitive reaction to probe the speciation of Ru surface sites. Propene and p-H_2 (3.8 mL s^{-1}, propene/p-H_2 = 1:4) were passed through a catalyst bed containing $Sm_2Ru_{0.2}Ce_{1.8}O_7$ while increasing the temperature from 100 to 500 °C and monitoring the conversion of propene and the NMR signal enhancement of propane due to the pairwise p-H_2 addition (weight-to-volume flow rate, W/F, was 0.24 ms g_{Ru} mL^{-1}, heating rate was 10 °C min^{-1}).[87,88] Under these conditions, $Sm_2Ru_{0.2}Ce_{1.8}O_7$ reaches the maximum of the propene conversion at 200 °C (55%) that decreases to 30% when increasing the temperature to 300 °C and further to 3% at 500 °C (Figure 3d). Hence, despite the increasing amount of exsolved metallic Ru with temperature (Figures 2b,e and 3a), the hydrogenation activity decreases, likely due to changes in the nature of Ru sites ($Ru^{\delta-}$ species and/or overcoat of the reduced support) at higher temperatures and, at least partially, due to the thermodynamics of the propene hydrogenation (exothermic reaction, Figure S22).[89] Note that a similar decline in the propene conversion of the supported Ir-based catalyst was explained by SMSI.[31] To further demonstrate that the discussed metal−support interactions modify significantly the nature of the Ru surface species, we have tested $Sm_2Ru_{0.2}Ce_{1.8}O_{7(500\text{-}H2)}$ (i.e., a catalyst that was pretreated in H_2 at 500 °C for 1 h) at low reaction temperatures and observed lower propene conversions compared to $Sm_2Ru_{0.2}Ce_{1.8}O_7$ that was reduced in situ at low reaction temperatures (Figure S23). This result confirms the role of MSI in the observed decrease in the hydrogenation activity. These MSI effects can be described by the geometric blocking of Ru sites by the reduced $Sm_2Ce_{1.8}O_{7-\delta}$ support,[60,90] as evidenced by XPS results (Figures S12, S13, and 3b), and/or a significantly higher activity of Ru^0 in propene hydrogenation relative to $Ru^{\delta-}$ sites. It is noteworthy that the NMR signal enhancement increased strongly at 500 °C, reaching a value of 95, which is an ca. 3-fold increase compared to the enhancement at 300 °C (Figure 3d). This points to a change

https://dx.doi.org/10.1021/acs.jpcc.0c07203
J. Phys. Chem. C 2020, 124, 25299−25307

of the hydrogen addition pathways or a change in the structure of the active sites. A similar increase of the pairwise addition after reduction at 500 °C was observed for Ir/TiO_2 and attributed to SMSI effects.[31] Our additional control experiments show that Ru-free $Ln_2Ce_2O_7$ (Ln = Sm, Nd, La) materials are inactive for the hydrogenation of propene under similar experimental conditions. That said, $Nd_2Ru_{0.2}Ce_{1.8}O_7$ and $La_2Ru_{0.2}Ce_{1.8}O_7$ display similar trends to $Sm_2Ru_{0.2}Ce_{1.8}O_7$ with regard to changes in the propene hydrogenation activity and the selectivity for pairwise addition with temperature (Figures S24 and S28).

Next, we probed the effect of the $Sm_2Ru_xCe_{2-x}O_7$ composition (x = 0.05, 0.1, 0.2, 0.4) on the catalytic activity in propene hydrogenation under similar reaction conditions. Independent of the reaction temperature, we observed an increase in the propene conversion (Figure S26a,b) and, respectively, a monotonic decrease in the NMR signal enhancement when increasing the Ru loading in the material (Figure S26c). For instance, at 300 °C, the propene conversion and NMR signal enhancements were 5% and 87-fold for $Sm_2Ru_{0.05}Ce_{1.95}O_7$, and 29% and 14-fold for $Sm_2Ru_{0.4}Ce_{1.6}O_7$, respectively. These data suggest a higher extent of the pairwise addition pathways on smaller supported Ru species, which are expected from the exsolution of $Sm_2Ru_{0.05}Ce_{1.95}O_7$ (material with 8-times lower nominal Ru content compared to $Sm_2Ru_{0.4}Ce_{1.6}O_7$).

MSI phenomena are known to be reversible, that is, the original state of the catalyst can be recovered upon reoxidation owing to the dissolution of the exsolved species.[91,92] Indeed, we observe that exposing $Ln_2Ru_{0.2}Ce_{1.8}O_{7(500\text{-}H2)}$ to static air at 500 °C for 1 h and retesting the oxidized catalyst under the same conditions lead, for all tested materials, to a recovery of the propene conversion (Figure S27) and NMR signal enhancement factors (Figure S28), as observed for the freshly calcined materials. These findings confirm the reversible nature of MSI effects discussed above.[31]

4. CONCLUSIONS

The catalytic properties of Ru-doped $Ln_2Ru_{0.2}Ce_{1.8}O_7$ (Ln = Sm, Nd, La) catalysts can be tailored rationally toward a higher activity or higher pairwise selectivity in propene hydrogenation through the triggering or avoiding of metal−support interactions (electronic and geometric) in the exsolved Ru species. In situ Ru K-edge XAS data uncovered that the reductive exsolution of Ru from $Sm_2Ru_{0.2}Ce_{1.8}O_7$ proceeds through an intermediate $Ru^{\delta+}$ state, i.e., $Ru^{4+}\rightarrow Ru^{\delta+}\rightarrow Ru^0$. XPS results demonstrated that the Ru^0/support interaction strengthens gradually with increasing reduction temperature (from 300 to 500 °C), accompanied by an increased coverage of the Ru^0 nanoparticles by the partially reduced support and an enhanced interfacial charge transfer that creates a $Ru^{\delta-}$ state. The selectivity of the pairwise addition of p-H_2 to propene is strongly dependent on the nature of the Ru sites. At 500 °C, a ca. 3-fold larger enhancement of the NMR signal of hyperpolarized propane is observed, which originates from the pairwise addition of p-H_2 to propene and is likely favored by the confinement effect and decreased hydride mobility, yet the propene conversion is low. In addition, the varying binding strengths of propene, propane, and key reaction intermediates on $Ru^{\delta-}$ and Ru^0 sites may also contribute to the observed increase in the pairwise selectivity of p-H_2 addition. This is also consistent with the presence of two types of Ru active sites that have diverging pairwise selectivity and deactivation by SMSI and/or EMSI such that less selective sites are deactivated to a larger extent. This increases the relative contribution of active sites more selective in p-H_2 pairwise addition to propene, leading to the observed higher signal enhancement. Overall, the catalytic activity of Ru^0 sites is significantly higher than that of $Ru^{\delta-}$ sites, but the selectivity for pairwise addition and hyperpolarization in the product is lower. These insights provide a guideline for a more rational synthesis of active and selective catalysts prepared by reductive exsolution.

■ ASSOCIATED CONTENT

Supporting Information

The Supporting Information is available free of charge at https://pubs.acs.org/doi/10.1021/acs.jpcc.0c07203.

Experimental details; XAS, XRD, Raman, XPS, and H_2-TPD data; STEM-EDX images; and catalytic activity results (PDF)

■ AUTHOR INFORMATION

Corresponding Authors

Alexey Fedorov − *Department of Mechanical and Process Engineering, ETH Zürich, CH 8092 Zürich, Switzerland;* orcid.org/0000-0001-9814-6726; Email: fedoroal@ethz.ch

Christoph R. Müller − *Department of Mechanical and Process Engineering, ETH Zürich, CH 8092 Zürich, Switzerland;* Email: muelchri@ethz.ch

Authors

Muhammad A. Naeem − *Department of Mechanical and Process Engineering, ETH Zürich, CH 8092 Zürich, Switzerland;* orcid.org/0000-0001-9026-5472

Dudari B. Burueva − *International Tomography Center, SB RAS, 630090 Novosibirsk, Russia; Novosibirsk State University, 630090 Novosibirsk, Russia;* orcid.org/0000-0002-6077-5487

Paula M. Abdala − *Department of Mechanical and Process Engineering, ETH Zürich, CH 8092 Zürich, Switzerland;* orcid.org/0000-0002-2011-1707

Nikolai S. Bushkov − *Department of Mechanical and Process Engineering, ETH Zürich, CH 8092 Zürich, Switzerland;* orcid.org/0000-0001-7803-6300

Dragos Stoian − *The Swiss−Norwegian Beamlines (SNBL) at ESRF, Grenoble 38043, France;* orcid.org/0000-0002-2436-6483

Andrey V. Bukhtiyarov − *Boreskov Institute of Catalysis, SB RAS, 630090 Novosibirsk, Russia;* orcid.org/0000-0002-0199-8111

Igor P. Prosvirin − *Novosibirsk State University, 630090 Novosibirsk, Russia; Boreskov Institute of Catalysis, SB RAS, 630090 Novosibirsk, Russia;* orcid.org/0000-0002-0351-5128

Valerii I. Bukhtiyarov − *Boreskov Institute of Catalysis, SB RAS, 630090 Novosibirsk, Russia*

Kirill V. Kovtunov − *International Tomography Center, SB RAS, 630090 Novosibirsk, Russia; Novosibirsk State University, 630090 Novosibirsk, Russia;* orcid.org/0000-0001-7577-9619

Igor V. Koptyug − *International Tomography Center, SB RAS, 630090 Novosibirsk, Russia; Novosibirsk State University, 630090 Novosibirsk, Russia;* orcid.org/0000-0003-3480-7649

https://dx.doi.org/10.1021/acs.jpcc.0c07203
J. Phys. Chem. C 2020, 124, 25299−25307

Complete contact information is available at:
https://pubs.acs.org/10.1021/acs.jpcc.0c07203

Notes

The authors declare no competing financial interest.

■ ACKNOWLEDGMENTS

The authors acknowledge the Scientific Center for Optical and Electron Microscopy (ScopeM) at ETH Zürich for the use of their electron microscopy facilities and Dr. A. Kierzkowska (ETH Zürich) for performing TEM analysis. ESRF and the Swiss Norwegian Beamlines (SNBL at ESRF) are gratefully acknowledged for providing access to the synchrotron facility. Financial support from the Competence Center of Energy and Mobility (CCEM), Swiss National Science Foundation R'Equip grant (4879135), Swiss Grid, Stiftung Claude & Giuliana, and the Swiss National Science Foundation (200020_156015) is greatly appreciated. V.I.B. and I.V.K. thank RSF (grant no: 19-13-00172) for the support of the catalyst characterization via XPS. D.B.B. and K.V.K. thank RFBR (19-29-10003 and 19-43-540004) and the Russian Ministry of Science and Higher Education (AAAA-A16-116121510087-5) for financial support.

■ REFERENCES

(1) Liu, L.; Corma, A. Metal Catalysts for Heterogeneous Catalysis: From Single Atoms to Nanoclusters and Nanoparticles. *Chem. Rev.* **2018**, *118*, 4981−5079.
(2) Pacchioni, G.; Freund, H.-J. Controlling the charge state of supported nanoparticles in catalysis: lessons from model systems. *Chem. Soc. Rev.* **2018**, *47*, 8474−8502.
(3) Dai, Y.; Lu, P.; Cao, Z.; Campbell, C. T.; Xia, Y. The physical chemistry and materials science behind sinter-resistant catalysts. *Chem. Soc. Rev.* **2018**, *47*, 4314−4331.
(4) Li, Z.; Ji, S.; Liu, Y.; Cao, X.; Tian, S.; Chen, Y.; Niu, Z.; Li, Y. Well-Defined Materials for Heterogeneous Catalysis: From Nanoparticles to Isolated Single-Atom Sites. *Chem. Rev.* **2020**, *120*, 623−682.
(5) Ro, I.; Resasco, J.; Christopher, P. Approaches for Understanding and Controlling Interfacial Effects in Oxide-Supported Metal Catalysts. *ACS Catal.* **2018**, *8*, 7368−7387.
(6) van Deelen, T. W.; Mejía, C. H.; de Jong, K. P. Control of metal-support interactions in heterogeneous catalysts to enhance activity and selectivity. *Nat. Catal.* **2019**, *2*, 955−970.
(7) Li, S.; Gong, J. Strategies for improving the performance and stability of Ni-based catalysts for reforming reactions. *Chem. Soc. Rev.* **2014**, *43*, 7245−7256.
(8) Zhang, Z.-c.; Xu, B.; Wang, X. Engineering nanointerfaces for nanocatalysis. *Chem. Soc. Rev.* **2014**, *43*, 7870−7886.
(9) Yang, Q.; Liu, G.; Liu, Y. Perovskite-Type Oxides as the Catalyst Precursors for Preparing Supported Metallic Nanocatalysts: A Review. *Ind. Eng. Chem. Res.* **2018**, *57*, 1−17.
(10) Munnik, P.; de Jongh, P. E.; de Jong, K. P. Recent Developments in the Synthesis of Supported Catalysts. *Chem. Rev.* **2015**, *115*, 6687−6718.
(11) Nishihata, Y.; Mizuki, J.; Akao, T.; Tanaka, H.; Uenishi, M.; Kimura, M.; Okamoto, T.; Hamada, N. Self-regeneration of a Pd-perovskite catalyst for automotive emissions control. *Nature* **2002**, *418*, 164.
(12) Neagu, D.; Tsekouras, G.; Miller, D. N.; Ménard, H.; Irvine, J. T. S. In situ growth of nanoparticles through control of non-stoichiometry. *Nat. Chem.* **2013**, *5*, 916.
(13) Kwon, O.; Sengodan, S.; Kim, K.; Kim, G.; Jeong, H. Y.; Shin, J.; Ju, Y.-W.; Han, J. W.; Kim, G. Exsolution trends and co-segregation aspects of self-grown catalyst nanoparticles in perovskites. *Nat. Commun.* **2017**, *8*, No. 15967.
(14) Millet, M.-M.; Tarasov, A. V.; Girgsdies, F.; Algara-Siller, G.; Schlögl, R.; Frei, E. Highly Dispersed $Ni^0/Ni_xMg_{1-x}O$ Catalysts Derived from Solid Solutions: How Metal and Support Control the CO_2 Hydrogenation. *ACS Catal.* **2019**, *9*, 8534−8546.
(15) Joo, S.; Kwon, O.; Kim, K.; Kim, S.; Kim, H.; Shin, J.; Jeong, H. Y.; Sengodan, S.; Han, J. W.; Kim, G. Cation-swapped homogeneous nanoparticles in perovskite oxides for high power density. *Nat. Commun.* **2019**, *10*, No. 697.
(16) Steiger, P.; Burnat, D.; Madi, H.; Mai, A.; Holzer, L.; Van Herle, J.; Kröcher, O.; Heel, A.; Ferri, D. Sulfur Poisoning Recovery on a Solid Oxide Fuel Cell Anode Material through Reversible Segregation of Nickel. *Chem. Mater.* **2019**, *31*, 748−758.
(17) Wu, Q.; Yan, B.; Cen, J.; Timoshenko, J.; Zakharov, D. N.; Chen, X.; Xin, H. L.; Yao, S.; Parise, J. B.; Frenkel, A. I.; Stach, E. A.; Chen, J. G.; Orlov, A. Growth of Nanoparticles with Desired Catalytic Functions by Controlled Doping-Segregation of Metal in Oxide. *Chem. Mater.* **2018**, *30*, 1585−1592.
(18) Pilger, F.; Testino, A.; Carino, A.; Proff, C.; Kambolis, A.; Cervellino, A.; Ludwig, C. Size Control of Pt Clusters on CeO_2 Nanoparticles via an Incorporation−Segregation Mechanism and Study of Segregation Kinetics. *ACS Catal.* **2016**, *6*, 3688−3699.
(19) Neagu, D.; Papaioannou, E. I.; Ramli, W. K. W.; Miller, D. N.; Murdoch, B. J.; Ménard, H.; Umar, A.; Barlow, A. J.; Cumpson, P. J.; Irvine, J. T. S.; Metcalfe, I. S. Demonstration of chemistry at a point through restructuring and catalytic activation at anchored nanoparticles. *Nat. Commun.* **2017**, *8*, No. 1855.
(20) Lu, J.; Zhu, C.; Pan, C.; Lin, W.; Lemmon, J. P.; Chen, F.; Li, C.; Xie, K. Highly efficient electrochemical reforming of CH_4/CO_2 in a solid oxide electrolyser. *Sci. Adv.* **2018**, *4*, No. eaar5100.
(21) Yan, B.; Wu, Q.; Cen, J.; Timoshenko, J.; Frenkel, A. I.; Su, D.; Chen, X.; Parise, J. B.; Stach, E.; Orlov, A.; Chen, J. G. Highly active subnanometer Rh clusters derived from Rh-doped $SrTiO_3$ for CO_2 reduction. *Appl. Catal., B* **2018**, *237*, 1003−1011.
(22) Xu, M.; He, S.; Chen, H.; Cui, G.; Zheng, L.; Wang, B.; Wei, M. TiO_{2-x}-Modified Ni Nanocatalyst with Tunable Metal−Support Interaction for Water−Gas Shift Reaction. *ACS Catal.* **2017**, *7*, 7600−7609.
(23) Liu, X.; Liu, M.-H.; Luo, Y.-C.; Mou, C.-Y.; Lin, S. D.; Cheng, H.; Chen, J.-M.; Lee, J.-F.; Lin, T.-S. Strong Metal−Support Interactions between Gold Nanoparticles and ZnO Nanorods in CO Oxidation. *J. Am. Chem. Soc.* **2012**, *134*, 10251−10258.
(24) Zhang, J.; Wang, H.; Wang, L.; Ali, S.; Wang, C.; Wang, L.; Meng, X.; Li, B.; Su, D. S.; Xiao, F.-S. Wet-Chemistry Strong Metal−Support Interactions in Titania-Supported Au Catalysts. *J. Am. Chem. Soc.* **2019**, *141*, 2975−2983.
(25) Ševčíková, K.; Szabová, L.; Kettner, M.; Homola, P.; Tsud, N.; Fabris, S.; Matolín, V.; Nehasil, V. Experimental and Theoretical Study on the Electronic Interaction between Rh Adatoms and CeO_x Substrate in Dependence on a Degree of Cerium Oxide Reduction. *J. Phys. Chem. C* **2016**, *120*, 5468−5476.
(26) Pan, C.-J.; Tsai, M.-C.; Su, W.-N.; Rick, J.; Akalework, N. G.; Agegnehu, A. K.; Cheng, S.-Y.; Hwang, B.-J. Tuning/exploiting Strong Metal-Support Interaction (SMSI) in Heterogeneous Catalysis. *J. Taiwan Inst. Chem. Eng.* **2017**, *74*, 154−186.
(27) Tauster, S. J. Strong metal-support interactions. *Acc. Chem. Res.* **1987**, *20*, 389−394.
(28) Hernández-Cristóbal, O.; Arenas-Alatorre, J.; Díaz, G.; Bahena, D.; J. Yacamán, M. High Resolution HAADF Characterization of Ir/TiO_2 Catalyst Reduced at 500 °C: Intensity Profile Analysis. *J. Phys. Chem. C* **2015**, *119*, 11672−11678.
(29) Kovtunov, K. V.; Barskiy, D. A.; Salnikov, O. G.; Burueva, D. B.; Khudorozhkov, A. K.; Bukhtiyarov, A. V.; Prosvirin, I. P.; Gerasimov, E. Y.; Bukhtiyarov, V. I.; Koptyug, I. V. Strong Metal−Support Interactions for Palladium Supported on TiO_2 Catalysts in the Heterogeneous Hydrogenation with Parahydrogen. *ChemCatChem* **2015**, *7*, 2581−2584.
(30) Li, W.; Zhang, G.; Jiang, X.; Liu, Y.; Zhu, J.; Ding, F.; Liu, Z.; Guo, X.; Song, C. CO_2 Hydrogenation on Unpromoted and M-Promoted Co/TiO_2 Catalysts (M = Zr, K, Cs): Effects of Crystal

Phase of Supports and Metal−Support Interaction on Tuning Product Distribution. *ACS Catal.* **2019**, *9*, 2739−2751.
(31) Zhao, E. W.; Zheng, H.; Ludden, K.; Xin, Y.; Hagelin-Weaver, H. E.; Bowers, C. R. Strong Metal−Support Interactions Enhance the Pairwise Selectivity of Parahydrogen Addition over Ir/TiO_2. *ACS Catal.* **2016**, *6*, 974−978.
(32) Tang, C.; Kousi, K.; Neagu, D.; Portolés, J.; Papaioannou, E. I.; Metcalfe, I. S. Towards efficient use of noble metals via exsolution exemplified for CO oxidation. *Nanoscale* **2019**, *11*, 16935−16944.
(33) Ciston, J.; Si, R.; Rodriguez, J. A.; Hanson, J. C.; Martínez-Arias, A.; Fernandez-García, M.; Zhu, Y. Morphological and Structural Changes during the Reduction and Reoxidation of CuO/CeO_2 and $Ce_{1-x}Cu_xO_2$ Nanocatalysts: In Situ Studies with Environmental TEM, XRD, and XAS. *J. Phys. Chem. C* **2011**, *115*, 13851−13859.
(34) Naeem, M. A.; Abdala, P. M.; Armutlulu, A.; Kim, S. M.; Fedorov, A.; Müller, C. R. Exsolution of Metallic Ru Nanoparticles from Defective, Fluorite-Type Solid Solutions $Sm_2Ru_xCe_{2-x}O_7$ To Impart Stability on Dry Reforming Catalysts. *ACS Catal.* **2020**, *10*, 1923−1937.
(35) Ortiz-Soto, L. B.; Monnier, J. R.; Amiridis, M. D. Structure-Sensitivity of Propylene Hydrogenation over Cluster-Derived Bimetallic Pt-Au Catalysts. *Catal. Lett.* **2006**, *107*, 13−17.
(36) Yang, J.-W.; Zheng, W.-T.; Hu, Z.; Zhang, M.; Xu, B.-Q. Do Olefin Hydrogenation Reactions Remain Structure Insensitive over Pt in Nanostructured Pt-on-Au Catalyst? *ACS Catal.* **2018**, *8*, 10254−10260.
(37) Kovtunov, K. V.; Beck, I. E.; Zhivonitko, V. V.; Barskiy, D. A.; Bukhtiyarov, V. I.; Koptyug, I. V. Heterogeneous addition of H_2 to double and triple bonds over supported Pd catalysts: a parahydrogen-induced polarization technique study. *Phys. Chem. Chem. Phys.* **2012**, *14*, 11008−11014.
(38) Salnikov, O. G.; Burueva, D. B.; Gerasimov, E. Y.; Bukhtiyarov, A. V.; Khudorozhkov, A. K.; Prosvirin, I. P.; Kovtunova, L. M.; Barskiy, D. A.; Bukhtiyarov, V. I.; Kovtunov, K. V.; Koptyug, I. V. The effect of oxidative and reductive treatments of titania-supported metal catalysts on the pairwise hydrogen addition to unsaturated hydrocarbons. *Catal. Today* **2017**, *283*, 82−88.
(39) Burueva, D. B.; Kovtunova, L. M.; Bukhtiyarov, V. I.; Kovtunov, K. V.; Koptyug, I. V. Single-Site Heterogeneous Catalysts: From Synthesis to NMR Signal Enhancement. *Chem. − Eur. J.* **2019**, *25*, 1420−1431.
(40) Tsoukalou, A.; Abdala, P. M.; Stoian, D.; Huang, X.; Willinger, M.-G.; Fedorov, A.; Müller, C. R. Structural Evolution and Dynamics of an In_2O_3 Catalyst for CO_2 Hydrogenation to Methanol: An Operando XAS-XRD and In Situ TEM Study. *J. Am. Chem. Soc.* **2019**, *141*, 13497−13505.
(41) Deeva, E. B.; Kurlov, A.; Abdala, P. M.; Lebedev, D.; Kim, S. M.; Gordon, C. P.; Tsoukalou, A.; Fedorov, A.; Müller, C. R. In Situ XANES/XRD Study of the Structural Stability of Two-Dimensional Molybdenum Carbide Mo_2CT_x: Implications for the Catalytic Activity in the Water−Gas Shift Reaction. *Chem. Mater.* **2019**, *31*, 4505−4513.
(42) Coduri, M.; Masala, P.; Allieta, M.; Peral, I.; Brunelli, M.; Biffi, C. A.; Scavini, M. Phase Transformations in the CeO_2−Sm_2O_3 System: A Multiscale Powder Diffraction Investigation. *Inorg. Chem.* **2018**, *57*, 879−891.
(43) Liu, Z.; Zhang, F.; Rui, N.; Li, X.; Lin, L.; Betancourt, L. E.; Su, D.; Xu, W.; Cen, J.; Attenkofer, K.; Idriss, H.; Rodriguez, J. A.; Senanayake, S. D. Highly Active Ceria-Supported Ru Catalyst for the Dry Reforming of Methane: In Situ Identification of $Ru^{\delta+}$−Ce^{3+} Interactions for Enhanced Conversion. *ACS Catal.* **2019**, *9*, 3349−3359.
(44) Ftouni, J.; Muñoz-Murillo, A.; Goryachev, A.; Hofmann, J. P.; Hensen, E. J. M.; Lu, L.; Kiely, C. J.; Bruijnincx, P. C. A.; Weckhuysen, B. M. ZrO_2 Is Preferred over TiO_2 as Support for the Ru-Catalyzed Hydrogenation of Levulinic Acid to γ-Valerolactone. *ACS Catal.* **2016**, *6*, 5462−5472.
(45) Tallarida, M.; Kukli, K.; Michling, M.; Ritala, M.; Leskelä, M.; Schmeisser, D. Substrate Reactivity Effects in the Atomic Layer Deposition of Aluminum Oxide from Trimethylaluminum on Ruthenium. *Chem. Mater.* **2011**, *23*, 3159−3168.
(46) Zhang, T.; Ge, Y.; Wang, X.; Chen, J.; Huang, X.; Liao, Y. Polymeric Ruthenium Porphyrin-Functionalized Carbon Nanotubes and Graphene for Levulinic Ester Transformations into γ-Valerolactone and Pyrrolidone Derivatives. *ACS Omega* **2017**, *2*, 3228−3240.
(47) Fan, L.; Sun, Q.; Zheng, W.; Tang, Q.; Zhang, T.; Tian, M. A Novel One-Step Hydrothermal Preparation of $Ru/Sn_xTi_{1-x}O_2$ Diesel Oxidation Catalysts and its Low-Temperature Performance. *Nanoscale Res. Lett.* **2020**, *15*, No. 109.
(48) Haga, M.-a.; Hong, H.-G.; Shiozawa, Y.; Kawata, Y.; Monjushiro, H.; Fukuo, T.; Arakawa, R. Synthesis and Proton-Coupled Electron-Transfer Reaction of Self-Assembled Monolayers of a Ruthenium(II) Complex Containing Tridentate 2,6-Bis-(benzimidazol-2-yl)pyridine on a Gold Surface: Comparison of Acid/Base Chemistry with Bulk Solution Chemistry. *Inorg. Chem.* **2000**, *39*, 4566−4573.
(49) Zubavichus, Y. V.; Slovokhotov, Y. L.; Nazeeruddin, M. K.; Zakeeruddin, S. M.; Grätzel, M.; Shklover, V. Structural Characterization of Solar Cell Prototypes Based on Nanocrystalline TiO_2 Anatase Sensitized with Ru Complexes. X-ray Diffraction, XPS, and XAFS Spectroscopy Study. *Chem. Mater.* **2002**, *14*, 3556−3563.
(50) Luo, W.; Sankar, M.; Beale, A. M.; He, Q.; Kiely, C. J.; Bruijnincx, P. C. A.; Weckhuysen, B. M. High performing and stable supported nano-alloys for the catalytic hydrogenation of levulinic acid to γ-valerolactone. *Nat. Commun.* **2015**, *6*, No. 6540.
(51) Moulder, J. F.; Stickle, W. F.; Sobol, P. E.; Bomben, K. D. *Handbook of X-Ray Photoelectron Spectroscopy: A Reference Book of Standard Spectra for Identification and Interpretation of XPS Data*; Perkin-Elmer Corporation Physical Electronics Division: Eden Prairie, MN, 1995.
(52) Lewera, A.; Timperman, L.; Roguska, A.; Alonso-Vante, N. Metal−Support Interactions between Nanosized Pt and Metal Oxides (WO_3 and TiO_2) Studied Using X-ray Photoelectron Spectroscopy. *J. Phys. Chem. C* **2011**, *115*, 20153−20159.
(53) Zhu, T.; Yang, M.; Chen, X.; Dong, Y.; Zhang, Z.; Cheng, H. A highly active bifunctional Ru−Pd catalyst for hydrogenation and dehydrogenation of liquid organic hydrogen carriers. *J. Catal.* **2019**, *378*, 382−391.
(54) Radnik, J.; Mohr, C.; Claus, P. On the origin of binding energy shifts of core levels of supported gold nanoparticles and dependence of pretreatment and material synthesis. *Phys. Chem. Chem. Phys.* **2003**, *5*, 172−177.
(55) Fang, M.; Machalaba, N.; Sánchez-Delgado, R. A. Hydrogenation of arenes and N-heteroaromatic compounds over ruthenium nanoparticles on poly(4-vinylpyridine): a versatile catalyst operating by a substrate-dependent dual site mechanism. *Dalton Trans.* **2011**, *40*, 10621−10632.
(56) Ogawa, T.; Kobayashi, Y.; Mizoguchi, H.; Kitano, M.; Abe, H.; Tada, T.; Toda, Y.; Niwa, Y.; Hosono, H. High Electron Density on Ru in Intermetallic YRu_2: The Application to Catalyst for Ammonia Synthesis. *J. Phys. Chem. C* **2018**, *122*, 10468−10475.
(57) Wang, Z.; Cai, Z.; Wei, Z. Highly Active Ruthenium Catalyst Supported on Barium Hexaaluminate for Ammonia Decomposition to COx-Free Hydrogen. *ACS Sustainable Chem. Eng.* **2019**, *7*, 8226−8235.
(58) Larichev, Y. V.; Moroz, B. L.; Zaikovskii, V. I.; Yunusov, S. M.; Kalyuzhnaya, E. S.; Shur, V. B.; Bukhtiyarov, V. I. XPS and TEM Studies on the Role of the Support and Alkali Promoter in Ru/MgO and Ru−Cs^+/MgO Catalysts for Ammonia Synthesis. *J. Phys. Chem. C* **2007**, *111*, 9427−9436.
(59) Abdel-Mageed, A. M.; Wiese, K.; Parlinska-Wojtan, M.; Rabeah, J.; Brückner, A.; Behm, R. J. Encapsulation of Ru nanoparticles: Modifying the reactivity toward CO and CO_2 methanation on highly active Ru/TiO_2 catalysts. *Appl. Catal., B* **2020**, *270*, No. 118846.
(60) Sato, K.; Miyahara, S.-i.; Ogura, Y.; Tsujimaru, K.; Wada, Y.; Toriyama, T.; Yamamoto, T.; Matsumura, S.; Nagaoka, K. Surface

https://dx.doi.org/10.1021/acs.jpcc.0c07203
J. Phys. Chem. C 2020, 124, 25299−25307

Dynamics for Creating Highly Active Ru Sites for Ammonia Synthesis: Accumulation of a Low-Crystalline, Oxygen-Deficient Nanofraction. *ACS Sustainable Chem. Eng.* **2020**, *8*, 2726−2734.
(61) Niwa, Y.; Aika, K. I. The promoter effect of lanthana on MgO supported ruthenium catalysts for ammonia synthesis. *Res. Chem. Intermed.* **1998**, *24*, 593−603.
(62) Li, W.; Wang, S.; Li, J. Highly Effective Ru/$BaCeO_3$ Catalysts on Supports with Strong Basic Sites for Ammonia Synthesis. *Chem. − Asian J.* **2019**, *14*, 2815−2821.
(63) Ma, Z.; Xiong, X.; Song, C.; Hu, B.; Zhang, W. Electronic metal−support interactions enhance the ammonia synthesis activity over ruthenium supported on Zr-modified CeO_2 catalysts. *RSC Adv.* **2016**, *6*, 51106−51110.
(64) Quan, F.; Zhan, G.; Mao, C.; Ai, Z.; Jia, F.; Zhang, L.; Gu, H.; Liu, S. Efficient light-driven CO_2 hydrogenation on Ru/CeO_2 catalysts. *Catal. Sci. Technol.* **2018**, *8*, 6503−6510.
(65) Tauster, S.; Fung, S.; Garten, R. L. Strong metal-support interactions. Group 8 noble metals supported on titanium dioxide. *J. Am. Chem. Soc.* **1978**, *100*, 170−175.
(66) Li, B.; Li, L.; Zhao, C. A highly stable Ru/$LaCO_3OH$ catalyst consisting of support-coated Ru nanoparticles in aqueous-phase hydrogenolysis reactions. *Green Chem.* **2017**, *19*, 5412−5421.
(67) Qiu, J.-Z.; Hu, J.; Lan, J.; Wang, L.-F.; Fu, G.; Xiao, R.; Ge, B.; Jiang, J. Pure Siliceous Zeolite-Supported Ru Single-Atom Active Sites for Ammonia Synthesis. *Chem. Mater.* **2019**, *31*, 9413−9421.
(68) Panagiotopoulou, P.; Kondarides, D. I.; Verykios, X. E. Mechanistic Study of the Selective Methanation of CO over Ru/TiO_2 Catalyst: Identification of Active Surface Species and Reaction Pathways. *J. Phys. Chem. C* **2011**, *115*, 1220−1230.
(69) Thang, H. V.; Tosoni, S.; Fang, L.; Bruijnincx, P.; Pacchioni, G. Nature of Sintering-Resistant, Single-Atom Ru Species Dispersed on Zirconia-Based Catalysts: A DFT and FTIR Study of CO Adsorption. *ChemCatChem* **2018**, *10*, 2634−2645.
(70) Chandra, D.; Inoue, Y.; Sasase, M.; Kitano, M.; Bhaumik, A.; Kamata, K.; Hosono, H.; Hara, M. A high performance catalyst of shape-specific ruthenium nanoparticles for production of primary amines by reductive amination of carbonyl compounds. *Chem. Sci.* **2018**, *9*, 5949−5956.
(71) Guglielminotti, E.; Bond, G. C. Effect of oxidation−reduction treatments on the infrared spectra of carbon monoxide chemisorbed on a Ru/TiO_2 catalyst. *J. Chem. Soc., Faraday Trans.* **1990**, *86*, 979−987.
(72) Hu, X.-C.; Fu, X.-P.; Wang, W.-W.; Wang, X.; Wu, K.; Si, R.; Ma, C.; Jia, C.-J.; Yan, C.-H. Ceria-supported ruthenium clusters transforming from isolated single atoms for hydrogen production via decomposition of ammonia. *Appl. Catal., B* **2020**, *268*, No. 118424.
(73) Loveless, B. T.; Buda, C.; Neurock, M.; Iglesia, E. CO Chemisorption and Dissociation at High Coverages during CO Hydrogenation on Ru Catalysts. *J. Am. Chem. Soc.* **2013**, *135*, 6107−6121.
(74) Li, J.; Liu, Z.; Cullen, D. A.; Hu, W.; Huang, J.; Yao, L.; Peng, Z.; Liao, P.; Wang, R. Distribution and Valence State of Ru Species on CeO_2 Supports: Support Shape Effect and Its Influence on CO Oxidation. *ACS Catal.* **2019**, *9*, 11088−11103.
(75) Faroldi, B. M.; Lombardo, E. A.; Cornaglia, L. M. Surface properties and catalytic behavior of Ru supported on composite La_2O_3−SiO_2 oxides. *Appl. Catal., A* **2009**, *369*, 15−26.
(76) Mizushima, T.; Tohji, K.; Udagawa, Y.; Ueno, A. An EXAFS and IR study of the CO adsorption-induced morphology change in ruthenium catalysts. *J. Am. Chem. Soc.* **1990**, *112*, 7887−7893.
(77) Chen, H.-T. First-Principles Study of CO Adsorption and Oxidation on Ru-Doped CeO_2(111) Surface. *J. Phys. Chem. C* **2012**, *116*, 6239−6246.
(78) Chin, S. Y.; Williams, C. T.; Amiridis, M. D. FTIR Studies of CO Adsorption on Al_2O_3- and SiO_2-Supported Ru Catalysts. *J. Phys. Chem. B* **2006**, *110*, 871−882.
(79) An, J.; Wang, Y.; Lu, J.; Zhang, J.; Zhang, Z.; Xu, S.; Liu, X.; Zhang, T.; Gocyla, M.; Heggen, M.; Dunin-Borkowski, R. E.; Fornasiero, P.; Wang, F. Acid-Promoter-Free Ethylene Methoxycarbonylation over Ru-Clusters/Ceria: The Catalysis of Interfacial Lewis Acid−Base Pair. *J. Am. Chem. Soc.* **2018**, *140*, 4172−4181.
(80) Chin, S. Y.; Alexeev, O. S.; Amiridis, M. D. Preferential oxidation of CO under excess H_2 conditions over Ru catalysts. *Appl. Catal., A* **2005**, *286*, 157−166.
(81) Kantcheva, M.; Sayan, S. On the mechanism of CO adsorption on a silica-supported ruthenium catalyst. *Catal. Lett.* **1999**, *60*, 27−38.
(82) Panagiotopoulou, P.; Verykios, X. E. Mechanistic Study of the Selective Methanation of CO over Ru/TiO_2 Catalysts: Effect of Metal Crystallite Size on the Nature of Active Surface Species and Reaction Pathways. *J. Phys. Chem. C* **2017**, *121*, 5058−5068.
(83) Chen, S.; Abdel-Mageed, A. M.; Gauckler, C.; Olesen, S. E.; Chorkendorff, I.; Behm, R. J. Selective CO methanation on isostructural Ru nanocatalysts: The role of support effects. *J. Catal.* **2019**, *373*, 103−115.
(84) Cíes, J. M.; del Río, E.; López-Haro, M.; Delgado, J. J.; Blanco, G.; Collins, S.; Calvino, J. J.; Bernal, S. Fully Reversible Metal Deactivation Effects in Gold/Ceria−Zirconia Catalysts: Role of the Redox State of the Support. *Angew. Chem., Int. Ed.* **2010**, *49*, 9744−9748.
(85) Liu, N.; Xu, M.; Yang, Y.; Zhang, S.; Zhang, J.; Wang, W.; Zheng, L.; Hong, S.; Wei, M. $Au^{\delta-}$−O_v−Ti^{3+} Interfacial Site: Catalytic Active Center toward Low-Temperature Water Gas Shift Reaction. *ACS Catal.* **2019**, *9*, 2707−2717.
(86) Sakamoto, H.; Ohara, T.; Yasumoto, N.; Shiraishi, Y.; Ichikawa, S.; Tanaka, S.; Hirai, T. Hot-Electron-Induced Highly Efficient O_2 Activation by Pt Nanoparticles Supported on Ta_2O_5 Driven by Visible Light. *J. Am. Chem. Soc.* **2015**, *137*, 9324−9332.
(87) Kovtunov, K. V.; Beck, I. E.; Bukhtiyarov, V. I.; Koptyug, I. V. Observation of Parahydrogen-Induced Polarization in Heterogeneous Hydrogenation on Supported Metal Catalysts. *Angew. Chem., Int. Ed.* **2008**, *47*, 1492−1495.
(88) Pokochueva, E.; Burueva, D.; Kovtunova, L.; Bukhtiyarov, A.; Gladky, A.; Kovtunov, K. V.; Koptyug, I. V.; Bukhtiyarov, V. Mechanistic in situ investigation of heterogeneous hydrogenation over Rh/TiO_2 catalysts: selectivity, pairwise route, catalyst nature. *Faraday Discuss.* **2020**, DOI: 10.1039/C9FD00138G.
(89) Sattler, J. J. H. B.; Ruiz-Martinez, J.; Santillan-Jimenez, E.; Weckhuysen, B. M. Catalytic Dehydrogenation of Light Alkanes on Metals and Metal Oxides. *Chem. Rev.* **2014**, *114*, 10613−10653.
(90) Ogura, Y.; Sato, K.; Miyahara, S.-i.; Kawano, Y.; Toriyama, T.; Yamamoto, T.; Matsumura, S.; Hosokawa, S.; Nagaoka, K. Efficient ammonia synthesis over a Ru/La0.5Ce0.5O1.75 catalyst pre-reduced at high temperature. *Chem. Sci.* **2018**, *9*, 2230−2237.
(91) Tang, H.; Su, Y.; Zhang, B.; Lee, A. F.; Isaacs, M. A.; Wilson, K.; Li, L.; Ren, Y.; Huang, J.; Haruta, M.; Qiao, B.; Liu, X.; Jin, C.; Su, D.; Wang, J.; Zhang, T. Classical strong metal−support interactions between gold nanoparticles and titanium dioxide. *Sci. Adv.* **2017**, *3*, No. e1700231.
(92) Bernal, S.; Calvino, J. J.; Cauqui, M. A.; Gatica, J. M.; López Cartes, C.; Pérez Omil, J. A.; Pintado, J. M. Some contributions of electron microscopy to the characterisation of the strong metal−support interaction effect. *Catal. Today* **2003**, *77*, 385−406.